ACS APPLIED MATERIALS & INTERFACES

Research Article

Cite This: ACS Appl. Mater. Interfaces 2019, 11, 9394−9404

www.acsami.org

Improving Photovoltaic and Enzymatic Sensing Performance by Coupling a Core−Shell Au Nanorod@TiO_2 Heterostructure with the Bioinspired L-DOPA Polymer

Linping Wang,[†] Yue Meng,[‡] Chunxiu Zhang,[†] Hongbo Xiao,[†] Yunlong Li,*[,†] Yueming Tan,[†] and Qingji Xie*[,†]

[†]Key Laboratory of Chemical Biology & Traditional Chinese Medicine Research (Ministry of Education of China), College of Chemistry and Chemical Engineering, Hunan Normal University, Changsha 410081, P.R. China

[‡]Institute of Nano-Bio Diagnosis and Therapy, College of Chemistry and Materials Engineering, Hunan University of Arts and Science, Changde 415000, China

Supporting Information

ABSTRACT: The photoelectrochemistry (PEC) performance of TiO_2 is somewhat limited by its wide band gap and low quantum efficiency, and the innovation of its composite materials provides a promising solution for an improved performance. Herein, a composite of a Au nanorod@TiO_2 core−shell nanostructure (AuNR@TiO_2) and a melanin-like L-DOPA polymer (PD) is designed and prepared, where the outer layer PD tethered by TiO_2-hydroxyl complexation and the AuNR core can intensify the long-wavelength light harvesting, and the AuNR@TiO_2 core−shell structure can strengthen the hot-electron transfer to TiO_2. The photocurrent of PD/AuNR@TiO_2 is 8.4-fold improved versus that of commercial TiO_2, and the maximum incident photon-to-electron conversion efficiency reaches 65% in the UV−visible−near-infrared region. In addition, the novel PD/AuNR@TiO_2 photocatalyst possesses the advantages of good biocompatibility and stability, which can act as a versatile PEC biosensing platform for providing a biocompatible environment and improving detection sensitivity. Herein, a PEC enzymatic biosensor of glucose is developed on the basis of the immobilization of dual enzyme [glucose oxidase (GOx) and horseradish peroxidase (HRP)] in PD and the signaling strategy of biocatalytic precipitation. In phosphate buffer containing glucose and 4-chloro-1-naphthol, the HRP-catalyzed oxidation of 4-chloro-1-naphthol by GOx-generated H_2O_2 can form a precipitate on the electrode, by which the decrement of photocurrent intensity is proportional to the common logarithm of glucose concentration. The linear detection range is from 0.05 μM to 10.0 mM glucose, with a limit of detection of 0.01 μM (S/N = 3). Glucose in some human serum samples is analyzed with satisfactory results.

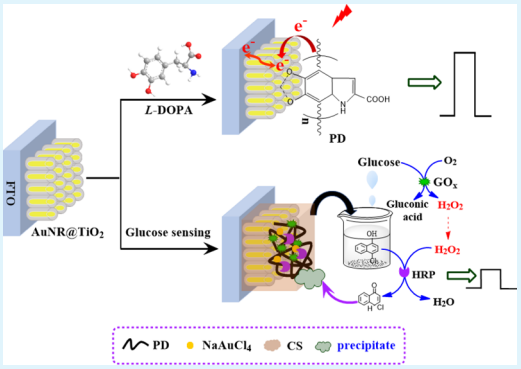

KEYWORDS: *Au nanorod@TiO_2 core−shell heterostructure, bioinspired L-DOPA polymer, photoelectrochemistry, biocatalytic precipitation, enzymatic sensing of glucose*

1. INTRODUCTION

The quantitative analysis of human blood glucose plays an important role in the fields of clinical diagnosis and health care especially on fighting diabetes mellitus.[1] The electrochemical biosensing of glucose has gained massive attention since 1960s.[2,3] Recently, photoelectrochemistry (PEC) creates a new era in prompting the development of biosensors.[4] Using light as the excitation source and photocurrent as the detection signal, PEC sensing features the advantages of low background signal, low cost, easy miniaturization, and high sensitivity.[5,6] The performance of PEC biosensors mainly relies on photovoltaic materials, which can act as light harvesting species to generate the electrical signals and/or as the recognition elements to biomolecular conjugation. The high biocompatibility of the materials is very important in bio-related PEC fields.[7] The PEC glucose sensors may be divided into two categories: nonenzymatic and enzymatic glucose sensors. The PEC nonenzymatic glucose sensors are mainly based on the photocatalytic oxidation of glucose. Glucose acted as an electron donor to react with the photogenerated holes or the redox-active molecules on the surface of photoelectrodes.[8,9] Gopalan et al. designed a nonenzymatic PEC glucose sensing platform by two-dimensional BiOCl-graphene nanohybrid sheets.[10] Devadoss et al. reported the direct PEC oxidation of glucose on a robust Cu_2O−TiO_2 electrode.[11] Other nonenzymatic PEC glucose sensors are also prepared using a core−shell WO_3@TiC−C composite,[12] ultrathin g-C_3N_4/WO_3 heterostructures,[13] a Ni/CdS/TiO_2

Received: November 3, 2018
Accepted: February 13, 2019
Published: February 13, 2019

DOI: 10.1021/acsami.8b19284
ACS Appl. Mater. Interfaces 2019, 11, 9394−9404

Scheme 1. Preparation Procedures and Sensing Principle for the PEC Glucose Biosensor

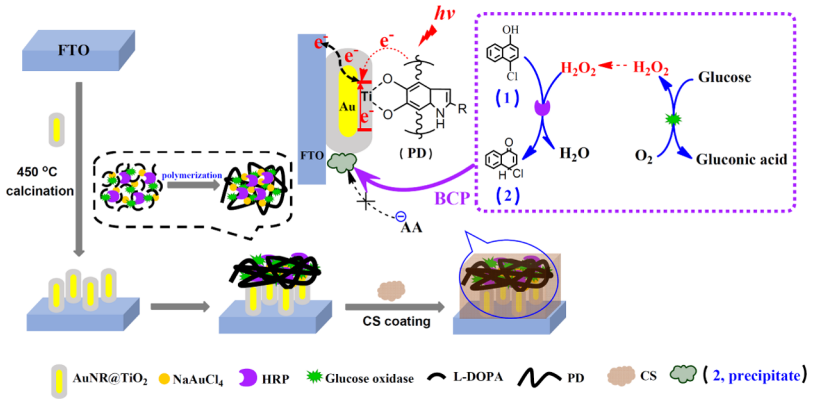

nanotube array,[14] and an amorphous MoS_x/reduced graphene oxide hybrid film.[15] The PEC-based enzymatic biosensors possess the advantages of enzymes' selectivity and PEC's sensitivity.[16−18] A variety of photoactive materials are used to immobilize enzymes for glucose detection, such as ZnS nanoparticles,[19] Ag_2S quantum dots,[20] ZnS−CdS hybrid quantum dots,[21] $TiO_2/CuInS_2/ZnS$ hybrids,[22] ZnO−Au@CdS microspheres,[23] and assembled $MoS_2−TiO_2$ heterostructures.[24] For enzymatic biosensors including PEC-based biosensors, how to efficiently maintain the enzymatic activity and prevent the enzyme leakage from the electrode surface is always an important issue.

As one of the most important photocatalytic materials, the TiO_2 photocatalyst has attracted much attention in PEC since 1972.[25,26] Tang et al. reported a sensitive enzymatic PEC biosensor for glucose by using TiO_2 nanowire-functionalized glucose oxidase (GOx) as the photoanode.[27] Li et al. prepared Ni−Cu nanoparticle-modified TiO_2 nanotube arrays for nonenzymatic glucose sensing.[28] Çakıroğlu et al. constructed a self-powered glucose biosensor by immobilizing GOx with the TiO_2−carbon nanotubes−Co_3O_4 hybrid semiconductor.[29] The photocatalytic efficiency of TiO_2 mainly depends on its chemical morphology, structure, size, surface area, and doping materials.[30] The single ingredient TiO_2 semiconductor often suffers the drawbacks of wide band gap, low visible-light absorption ability, and easy recombination of photogenerated electron−hole (e−h) pairs.[31] The surface plasmon resonance (SPR) of noble metals (e.g., Au and Ag) can largely improve the charge separation and transfer of the TiO_2 semiconductor by injecting "hot" electrons over the interfacial Schottky barrier.[32−34] Many plasmonic PEC biosensors for glucose detection have been fabricated by metal−semiconductor systems, such as Au−TiO_2-patterned heterostructures,[35] hollow nano Ag&Pt−TiO_2,[36] Pt−TiO_2,[37] graphene−WO_3−Au hybrid membranes,[38] and Au−CuS−TiO_2 nanocomposites.[39] Compared with common metal−semiconductor systems, core−shell metal@semiconductor materials have emerged as powerful materials in the study of surface-enhanced light-harvesting processes with the advantages of improved physicochemical properties, including versatility, tunability, stability, and dispersibility.[40] The Au nanorod (AuNR) material is a suitable candidate for fabricating the core−shell metal@semiconductor composite because of its tunable longitudinal localized SPR band, which can vary from the visible to near-infrared (NIR) region by tailoring the length-to-diameter aspect ratio.[41] The unique anisotropic character of AuNRs can make it assembled into numerous superstructures.[42] Hence, the controllable preparation of AuNR@TiO_2 core−shell structures can maximize the charge transportation/separation ability of TiO_2 and enhance the photocatalytic efficiency over almost the entire solar spectrum.[43]

The artificial synthesis of biomimetic materials has emerged as a promising tool to provide biocompatible environments of materials.[44,45] Typically, polydopamine (PDA) is a biomimetic polymer material inspired from mussel adhesion proteins, attracting much attention in the study of biocompatible coating, solar cells, and surface modifications.[46−50] Ryu et al. used PDA to immobilize Nile Blue redox mediators on the surface of Fe_2O_3/fluorine-doped tin oxide (FTO) electrodes, which acted as a versatile PEC enzymatic platform for glucose sensing.[51] Nam et al. reported a new synthetic PDA dye as an efficient photosensitizer for TiO_2-based solar cells, which can extend the absorption of TiO_2 into the visible region.[52] PDA may strongly bind with TiO_2 through residual −OH groups of the catechol moiety and form a strong bidentate complex to promote the transfer of photoexcited electrons of PDA to the conduction band of TiO_2.[52] 3-(3,4-Dihydroxyphenyl)-L-alanine (L-DOPA) is a structurally similar compound of dopamine (DA), which plays an important role in the process of tyrosinase catalysis of the oxidation of L-tyrosine to form melanin.[53] Learning from melanin, L-DOPA polymer (PD) is suggested as a special amino acid polymer with additional pending −COOH groups on its backbone for enzyme immobilization and amperometric biosensing.[54−56] Thus, PD can be a good candidate to match PDA as an efficient PEC photocatalyst, which offers a highly biocompatible matrix for convenient surface functionalization, biological interactions, and film-coating applications.[57] In general, there are three approaches to the synthesis of PD: chemical oxidation, electrochemical oxidation, and enzyme-catalyzed oxidation.[58,59] In this regard, PD is a promising biomimetic polymer that can be further explored in PEC enzymatic biosensors. The first generation of PEC enzymatic biosensors has been widely studied, which utilizes cosubstrate O_2 (or the generated H_2O_2) as the electron acceptor (or donor).[60−62] It has been reported that the enzyme-based biocatalytic precipitation (BCP) strategy can be employed in PEC sensors for lowering the detection limits and the competitively nonproductive absorption of enzymes.[63,64] Many oxidases (e.g., GOx, lactate oxidase, and choline oxidase) involve the oxidation of the respective substrates by O_2, generating H_2O_2 that can stimulate the BCP process.[65] Thus, the assembling of enzyme electrodes with the BCP strategy to alter the interface electrical features of PEC

DOI: 10.1021/acsami.8b19284
ACS Appl. Mater. Interfaces 2019, 11, 9394−9404

transducers is a competitive signal amplification strategy to apply in various PEC biosensors.

Herein, a composite is first prepared by coating bioinspired PD on the core−shell AuNR@TiO_2 nanostructure (PD/AuNR@TiO_2), which exhibits a broader absorption from UV−visible to NIR, enhanced separation of e−h pairs, high photoelectric conversion efficiency, and good biocompatibility. Meanwhile, a multiamplified PEC sensor for glucose is constructed by the novel PD/AuNR@TiO_2 composite photocatalyst combined with a dual enzyme-involved BCP strategy, with GOx as a H_2O_2-generating enzyme and horseradish peroxidase (HRP) as a product-precipitating enzyme. As shown in Scheme 1, the AuNR@TiO_2 core−shell heterostructure is synthesized by the wet-chemistry method and calcined to change the structure from the amorphous TiO_2 to anatase phase. PD is employed as an ideal polymer for enzymes' immobilization, which can well maintain the bioactivity of enzymes. GOx and HRP are co-entrapped in PD that is formed by the oxidation of L-DOPA in the presence of $NaAuCl_4$, followed by chitosan (CS) coating to stabilize the HRP−GOx−Au−PD bioconjugate on the FTO surface. The dual enzyme-involved BCP strategy is realized upon HRP-catalyzed oxidation of 4-chloro-1-naphthol by GOx-generated H_2O_2 to yield a precipitate, which inhibits the interfacial electron transfer of the electron donor (ascorbic acid, AA). Accordingly, a high-performance PEC enzymatic biosensor is constructed for glucose analysis by the combination of multisignal amplifiers (AuNR@TiO_2 core−shell structure, bioinspired PD, and HRP−GOx dual-enzyme) with the favorable BCP quenching process. The glucose analysis in some human serum samples is achieved by completing the BCP process out of the detection cell and then by PEC detection, which can avoid the direct exposure of blood samples to light illumination. This new PEC sensing platform exhibits enhanced photovoltaic performance, high detection sensitivity, low detection limit, and well-maintained enzyme activity.

2. EXPERIMENTAL SECTION

2.1. Reagents and Materials. GOx (EC 1.1.3.4, type II from *Aspergillus niger*, 150 U mg^{-1}), HRP (EC 1.11.1.7, 300 U mg^{-1}), L-DOPA, CS from crab shells (90% deacetylated), and 4-chloro-1-naphthol were purchased from Sigma-Aldrich. $TiCl_3$ (15−20%), tetrachloroaurate trihydrate ($HAuCl_4{\cdot}3H_2O$), hexadecyltrimethylammonium bromide (CTAB), sodium oleate (NaOL), sodium dodecyl sulfate (SDS), AA, and glucose were purchased from Sinopharm Chemical Reagent Co., Ltd (Shanghai, China). All other chemicals were of analytical grade or better quality. The FTO slices (type P003, sheet resistance <15 Ω/cm^2) were purchased from Zhuhai Kaivo Optoelectronic Technology Co., Ltd. (Zhuhai, China). pH 7.0 phosphate buffer solution (PBS, NaH_2PO_4−Na_2HPO_4, 30.0 mM) was used in the glucose detection process; 0.1 M pH 7.4 PBS was used in the L-DOPA polymerization process; and Milli-Q ultrapure water (Millipore, ≥18 MΩ cm) was used throughout. Human blood sera were kindly donated by Hunan Normal University Hospital.

2.2. Apparatus. PEC experiments were performed on an electrochemical workstation (ZENNIUM, ZAHNER-elektrik GmbH & Co. KG, Germany) equipped with a PEC setup (CIMPS, PP211, ZAHNER-elektrik GmbH & Co. KG, Germany). The light source (WLC02, ZAHNER-elektrik GmbH & Co. KG, Germany) was calibrated to 1 Sun (100 mW cm^{-2}). The incident photon-to-electron conversion efficiency (IPCE) was measured with a tunable light source (TLS03) from 365 to 1024 nm at a bias of 0.85 V. FTO electrodes were used as the working electrode (0.25 cm^2 area), a KCl-saturated calomel electrode (SCE) as the reference electrode, and a Pt disk electrode as the counter electrode. The electrochemical experiments were conducted on a CHI660C electrochemical workstation (CH Instruments Inc., Austin, TX) by using a graphite rod (4 mm diameter, 1.5 cm length) as the counter electrode and an SCE as the reference electrode. Characterizations of transmission electron microscopy (TEM) and high-resolution TEM (HRTEM) were performed on a FEI Tecnai G2 F20 transmission electron microscope, which is equipped with an Oxford energy-dispersive X-ray spectroscopy (EDX) analysis detector for elemental analysis. Scanning electron microscopy (SEM) characterizations were performed on a FEI Helios NanoLab 600i scanning electron microscope. X-ray diffraction (XRD) patterns were collected on a Rigaku RAPID IIR diffractometer with Cu Kα radiation operated at 40 kV, 250 mA at a step size of 1°. Dynamic light scattering (DLS, Malvern Zetasizer Nano ZS) was used to measure the size of AuNR. UV−vis spectrophotometry was conducted on a UV-2450 ultraviolet−visible spectrophotometer (Shimadzu, Japan).

2.3. Synthesis of AuNRs. The AuNRs were prepared by a modified seed-growth method reported by Nikoobakht and El-Sayed.[66] First, Au seed solution was prepared by rapidly adding ice-cooled 0.6 mL of 0.1 M aqueous $NaBH_4$ into an aqueous solution containing 10 mL of 0.1 M CTAB and 0.1 mL of 25 mM $HAuCl_4$. The mixed solution was stirred for 2 min and left for 30 min at 30 °C before use.

For AuNR synthesis, 0.8 mL of 25 mM $HAuCl_4$ was mixed with 20 mL aqueous solution containing 0.1 M CTAB and 16 mM NaOL by vortex mixing in a 30 °C water bath for 90 min. After adding 150 μL of concentrated HCl to adjust the solution pH, 64 μL of 0.1 M AA and 0.75 mL of 10 mM $AgNO_3$ were added sequentially into the CTAB−NaOL−$HAuCl_4$ solution. Immediately, 16 μL of seed solution was added and stirred for 30 s, followed by being undisturbed for 12 h in a 30 °C water bath. The final product was centrifuged at 8000 rpm and then 5000 rpm for 20 min, respectively. Finally, the AuNRs were redispersed in 10 mL of H_2O for further use.

2.4. Synthesis of AuNR@TiO_2 Heterostructures. The cationic surfactant-encapsulated AuNRs were first exchanged with the SDS anionic surfactant. AuNRs (0.5 mL) were mixed with 20 mL of 0.1 M SDS solution for 30 min. Then, AuNRs were collected by centrifuging at 8000 rpm twice to remove the excess surfactant and redispersed in 10 mL water for TiO_2 coating.

For the synthesis of AuNR@TiO_2 core−shell heterostructures, 0.2 mL of $TiCl_3$ solution (17.1 wt %, containing 20−30 wt % HCl) was diluted with 4 mL of H_2O. Then, 0.8 mL of 1 M $NaHCO_3$ solution was dropped in $TiCl_3$ solution under stirring. Before the solution turned into dark blue, the SDS-encapsulated AuNRs were added into the solution immediately, and kept stirring for 30 min at room temperature. The product was washed twice with ethanol, centrifuged at 6000 rpm for 10 min, and redispersed in water before use.

2.5. Fabrication of PD/AuNR@TiO_2/FTO. Electrochemical oxidative polymerization of L-DOPA on the AuNR@TiO_2/FTO electrode was prepared by immersing the AuNR@TiO_2/FTO electrode in a stirred PBS (pH 7.4) containing 10 mM L-DOPA for 20-cycle potential sweeps from −1.0 to 1.0 V at a scan rate of 50 mV/s.

2.6. Synthesis of HRP−GOx−Au−PD Bionanocomposite. The HRP−GOx−Au−PD bionanocomposite was synthesized by adding 2 mM $NaAuCl_4$ in PBS containing 6 mg mL^{-1} HRP, 6 mg mL^{-1} GOx, and 40 mM L-DOPA for stirred 4 h. After the polymerization, the solution became dark in color with the precipitate formed. Then, the HRP−GOx−Au−PD precipitate was centrifuged and redispersed in PBS before use.

2.7. Electrode Modifications and Biosensing. Prior to modification, FTO electrodes were cleaned by ultrasonication successively in acetone, ethanol, and water each for 15 min, and then dried in oven. 20 μL of AuNR@TiO_2 aqueous dispersion was dropped onto a cleaned FTO electrode and calcined at 450 °C for 3 h to change the structure from the amorphous TiO_2 shell to anatase phase. Subsequently, 10 μL of the resulting HRP−GOx−Au−PD bionanocomposite was cast on the obtained AuNR@TiO_2/FTO electrode and allowed for solvent evaporation. Finally, 8 μL of 0.2 wt

DOI: 10.1021/acsami.8b19284
ACS Appl. Mater. Interfaces 2019, 11, 9394−9404

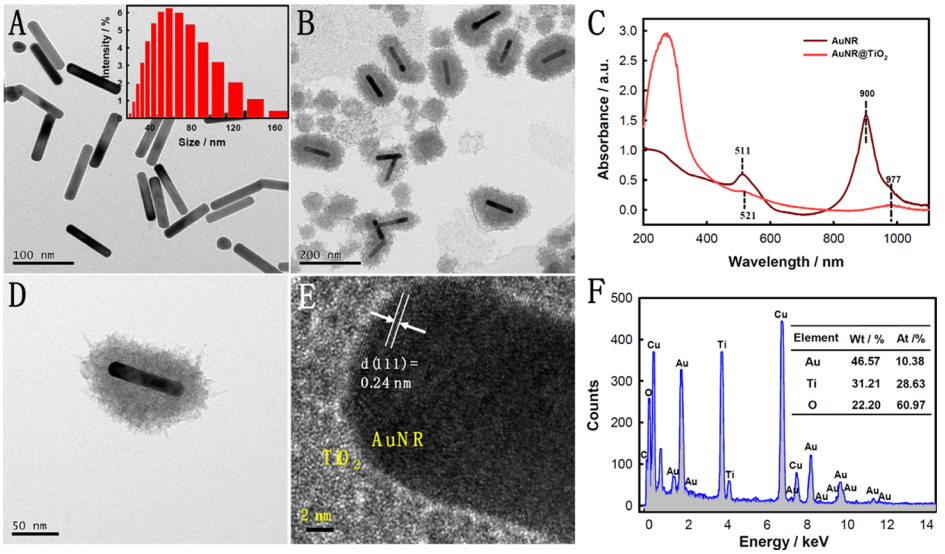

Figure 1. TEM images of uncoated AuNRs [(A); inset: DLS spectrum], AuNR@TiO_2 core−shell composites (B), and their UV−vis spectra (C). Single AuNR@TiO_2 core−shell nanostructure's TEM (D), HRTEM (E), and EDX spectrum (F).

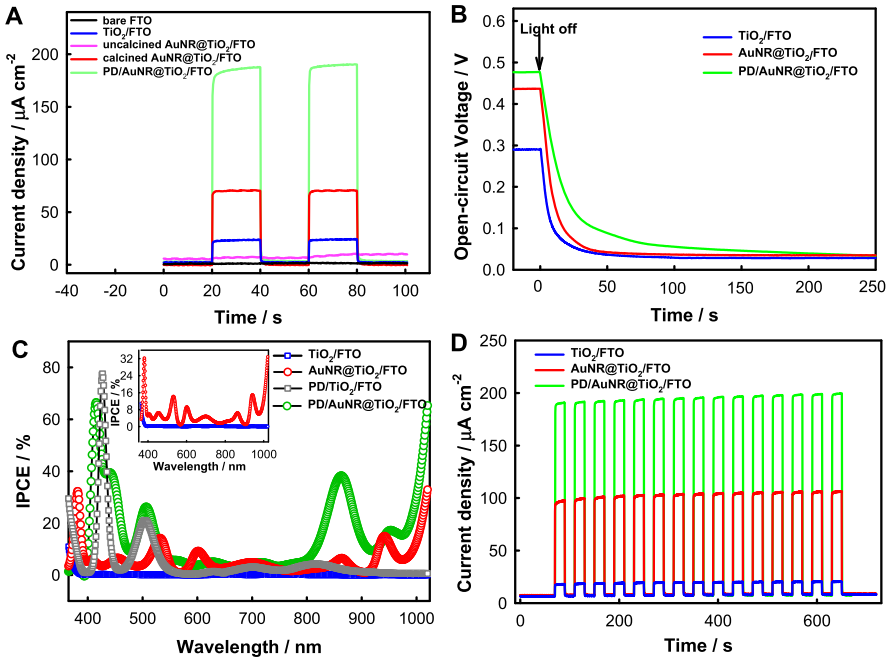

Figure 2. (A) Photocurrent responses of bare FTO, TiO_2/FTO, uncalcined and calcined AuNR@TiO_2/FTO, as well as PD/AuNR@TiO_2/FTO electrodes. (B) V_{OC}−t curves of the TiO_2-, AuNR@TiO_2-, and PD/AuNR@TiO_2-modified FTO electrodes. (C) IPCE spectra of the TiO_2/FTO, AuNR@TiO_2/FTO, PD/TiO_2/FTO, and PD/AuNR@TiO_2/FTO films. (D) Photostability of TiO_2/FTO, AuNR@TiO_2/FTO, and PD/AuNR@TiO_2/FTO.

% CS solution was cast on HRP−GOx−Au−PD/AuNR@TiO_2/FTO and dried naturally.

For glucose sensing, CS/HRP−GOx−Au−PD/AuNR@TiO_2/FTO was incubated in PBS (pH = 7.0) containing 1 mM 4-chloro-1-naphthol and glucose at a certain concentration for 20 min at 37 °C to complete the BCP reaction. Then, the PEC measurement was then carried out in PBS (pH = 7.0) containing 0.1 M AA as the sacrificial electron donor.

3. RESULTS AND DISCUSSION

3.1. Morphology and Structure of AuNR and AuNR@TiO_2 Core−Shell Nanocomposites. Synthesized AuNR and AuNR@TiO_2 were characterized by TEM. The average size of the materials is obtained by counting 30 nanorods. As shown in Figure 1A, the average diameter and length of the AuNR are 18 ± 2 and 95 ± 7 nm, respectively, with an average aspect ratio of 5.3. The dominant DLS size of AuNRs is about 60 nm (inset of Figure 1A), which is acceptably consistent with the sizes of AuNRs obtained from TEM. Note that because of the rod shape, the diameter from DLS measurement is not the actual size of the NRs.[67] The core−shell AuNR@TiO_2 exhibits a rodlike structure and good monodispersity, along with few byproducts, as shown in Figure 1B. The average thickness of the TiO_2 shell around the AuNR core is ca. 38 ± 8 nm on the side and ca. 41 ± 7 nm on the end. The UV−vis absorption spectra of AuNR and AuNR@TiO_2 also confirm the successful

DOI: 10.1021/acsami.8b19284
ACS Appl. Mater. Interfaces 2019, 11, 9394−9404

synthesis of the AuNR@TiO_2 core−shell nanostructure, as shown in Figure 1C. A longitudinal absorption peak of the AuNR appears at 900 nm, and a transverse absorption peak appears at 511 nm, indicating the successful synthesis of rodlike AuNRs as reported previously.[66] After coating with TiO_2, the longitudinal and transverse absorption peaks of core−shell AuNR@TiO_2 red shift to 977 and 521 nm, respectively. The results reveal that TiO_2 is successfully coated on the AuNR, which can enhance the refractive index of the surrounding medium.[68] A single AuNR@TiO_2 core−shell nanostructure was further characterized by TEM (Figure 1D), HRTEM (Figure 1E), and EDX (Figure 1F). Both TEM and HRTEM images of single AuNR@TiO_2 show the distinct core−shell interface between AuNR and TiO_2. From HRTEM, the AuNR core shows a lattice spacing of 0.24 nm, which corresponds to the (111) plane of Au. Besides, the TiO_2 shell is amorphous because of the wet-chemistry synthesis of AuNR@TiO_2 at room temperature. These results are consistent with the findings of XRD patterns of amorphous AuNR@TiO_2 composites and calcined AuNR@TiO_2, as shown in Figure S1. The amorphous AuNR@TiO_2 only shows diffraction peaks of the cubic Au phase (JCPDS no. 04-0784) while the calcined AuNR@TiO_2 shows both diffraction peaks of Au and anatase TiO_2 (JCPDS no. 21-1272). Thus, the AuNR@TiO_2 core−shell structure is successfully synthesized, and the amorphous TiO_2 shell turns to the anatase phase by calcination. The EDX spectrum of single AuNR@TiO_2 further indicates that Au, Ti, and O elements are distributed on the single AuNR@TiO_2 composite (Figure 1F). The atom percentages of Ti and O are 28.63 and 60.97%, respectively, indicating the formation of the TiO_2 shell on AuNRs.

3.2. Photoelectrochemical Studies. We investigated the photovoltaic performances of TiO_2-, AuNR@TiO_2-, and PD/AuNR@TiO_2-modified FTO electrodes, as shown in Figure 2. Figure 2A shows the photocurrent responses of bare FTO, TiO_2/FTO, and uncalcined/calcined AuNR@TiO_2/FTO as well as PD/AuNR@TiO_2/FTO. For bare FTO and uncalcined AuNR@TiO_2/FTO electrodes, almost no photocurrent responses were observed. In contrast, a photocurrent density of about 70.3 μA cm^{-2} was obtained at the calcined AuNR@TiO_2/FTO electrode. The dramatically increased photocurrent is attributed to the structure of the amorphous TiO_2-shell change to the anatase phase by calcination. Meanwhile, the AuNR@TiO_2 core−shell structure can efficiently accelerate the interfacial charge transfer processes by sharing "hot" electrons at the metal−semiconductor core−shell interface. AuNR-free TiO_2/FTO exhibits a small photocurrent density of 21.6 μA cm^{-2}, while the photocurrent density of PD/AuNR@TiO_2/FTO is about 182 μA cm^{-2}. The photocurrent density of PD/AuNR@TiO_2/FTO is about 8.4-folds that of TiO_2/FTO, and 2.6-folds that of AuNR@TiO_2/FTO. The improvement of the photocurrent density of PD/AuNR@TiO_2/FTO is attributed to the PD photosensitizer tethered on the TiO_2-shell by Ti−ligand complexation. The synergistic effect of the AuNR@TiO_2 core−shell structure with the TiO_2−PD complex can provide a significant enhancement of TiO_2 charge separation. The possible interfacial electron transfer mechanisms of the PEC transducer upon light excitation is shown in Figure S2. Under irradiation, PD triggers the highest occupied molecular orbital (HOMO) and the lowest unoccupied molecular orbital (LUMO) by its $\pi-\pi$ system, which makes electrons transfer from the HOMO to LUMO. Then, the electron injection occurs from the LUMO energy level of PD to the conduction band of TiO_2 as previously reported.[52] Meanwhile, AuNR@TiO_2 core−shell nanostructures can effectively improve electron generation and transformation through a metal plasmon sensitization mechanism. The plasmonic AuNR can generate "hot" electrons and inject them into the conduction band of the TiO_2 semiconductor over a Schottky barrier, which is formed at the interface between the AuNR-core and TiO_2-shell.[68] When the electron donor (AA) exists in the solution, the photogenerated holes immigrate into the solution in which they oxidize AA and the e−h recombination can be effectively avoided.

Figure 2B shows the open circuit voltage−time ($V_{OC}-t$) curves of TiO_2/FTO, AuNR@TiO_2/FTO, and PD/AuNR@TiO_2/FTO electrodes under the turn-off condition after continuous illumination. The V_{OC} values of TiO_2/FTO, AuNR@TiO_2/FTO, and PD/AuNR@TiO_2/FTO are 0.288, 0.436, and 0.477 V versus SCE, respectively. The V_{OC} value of AuNR@TiO_2/FTO is larger than that of TiO_2/FTO, indicating that core−shell AuNR@TiO_2 generates more electrons by sharing "hot" electrons. The maximal V_{OC} value of PD/AuNR@TiO_2/FTO further confirms that PD can inhibit the e−h recombination by transferring its π electrons to the conduction band of TiO_2. When the light is switched off, the transient decay of V_{OC} can be used to evaluate the electron lifetime in the conduction band of TiO_2. According to the Bisquert equation[69]

$$\tau_n = -\left(\frac{k_B T}{e}\right)\left(\frac{dV_{OC}}{dt}\right)^{-1}$$

where τ_n, k_B, T, e, and t are the decay electron lifetime, Boltzmann's constant, temperature, charge of a single electron, and time, respectively. The slow decay of the $V_{OC}-t$ curve represents the longer electron lifetime and a low proportion of e−h recombination centers at the sample surface. The photoinduced electron lifetime follows the order PD/AuNR@TiO_2/FTO > AuNR@TiO_2/FTO > TiO_2/FTO. Thus, both PD and AuNR in the PD/AuNR@TiO_2 photocatalyst could help the transfer of TiO_2 electrons to the electrode surface and inhibit the recombination of e−h pairs.

The IPCE spectra of TiO_2/FTO, AuNR@TiO_2/FTO, PD/TiO_2/FTO, and PD/AuNR@TiO_2/FTO electrodes are shown in Figure 2C. The IPCE is approximately 10% for the anatase TiO_2 at ca. 365 nm, while AuNR@TiO_2/FTO shows good responses in both UV−visible and NIR ranges, with maximum values of approximately 32%. The plasmonic effect and longitudinal localized SPR band of the AuNR-core yield higher photocurrent responses than that of anatase TiO_2. Compared with PD/TiO_2/FTO, the IPCE of PD/AuNR@TiO_2/FTO also exhibits enhanced photocurrent and a broadened light absorption across the NIR region, where the maximum IPCE is approximately 65%. These observations represent that the efficiency of hot electron generation of AuNR-core by SPR can improve charge carrier transport through the interface of TiO_2. Incorporated with PD, the IPCE value of PD/TiO_2/FTO and PD/AuNR@TiO_2/FTO are further enhanced with a remarkable red shift in UV absorption due to the formation of conjugated π-electrons on the surface of the TiO_2-shell. This phenomenon is consistent with the UV−vis absorption spectra, as shown in Figure S3. The electropolymerized PD/FTO exhibits broad absorption peaks at 280 nm. AuNR@TiO_2/FTO exhibits the TiO_2 absorption peak at 316 nm and two small absorption peaks of AuNR at

DOI: 10.1021/acsami.8b19284
ACS Appl. Mater. Interfaces 2019, 11, 9394−9404

550 and 1024 nm, respectively. The UV peak of PD in PD/AuNR@TiO_2/FTO red shifts to 420 nm with wide absorption (vs 280 nm), indicating the formation of conjugated π-electrons between PD and TiO_2-shell.

The photostability of the synthesized core−shell AuNR@TiO_2 composite and PD/AuNR@TiO_2/FTO electrode in contrast to TiO_2/FTO was also studied by continuous light illumination in 0.1 M AA, as shown in Figure 2D. The photocurrent was almost unchanged over 15 repeated ON/OFF switching, revealing the good stability of the prepared electrodes.

3.3. Photoelectrochemical Biosensing of glucose. The chemical polymerization of L-DOPA is conducted by using $NaAuCl_4$ as a chemical oxidant in the presence of GOx and HRP, and characterized by TEM and UV−vis spectroscopy, as shown in Figure S4. The TEM image of the HRP−GOx−Au−PD bionanocomposite shows many Au nanoparticles of ca. 6 nm diameter entrapped in the melanin-like polymer. UV−vis absorption spectra confirm the formation of the HRP−GOx−Au−PD bionanocomposite. The GOx, HRP, L-DOPA, and $NaAuCl_4$ solutions show their absorption peaks at ca. 278, 401, 263, and 305 nm, respectively. After adding $NaAuCl_4$ in the GOx + HRP + L-DOPA solution for 4 h reaction, the black HRP−GOx−Au−PD precipitate was formed, and the UV−vis absorption peaking at 280 and 400 nm implies the successful polymerization of L-DOPA that can immobilize HRP and GOx enzymes.

The fabrication process of the PEC glucose sensor was also monitored by SEM, as shown in Figure 3. Bare FTO shows a scalelike rough surface due to the fluorine-doped SnO_2 layer deposited on the glass surface (Figure 3A). Figure 3B depicts the SEM image of the AuNR@TiO_2/FTO electrode after calcination at 450 °C for 4 h. The rodlike AuNR@TiO_2 structures change to massive heterostructures after calcination, which can compactly incorporate AuNR@TiO_2 rods through atom packing. After casting the HRP−GOx−Au−PD polymer on AuNR@TiO_2/FTO, a flakelike rough film is seen (Figure 3C). After CS coating, the CS/HRP−GOx−Au−PD/AuNR@TiO_2/FTO electrode exhibits a glue-applied film (Figure 3D). Figure 3E shows the CS/HRP−GOx−Au−PD/AuNR@TiO_2/FTO electrode after the BCP process by adding a glucose analyte. It can be seen that the precipitates are generated on the electrode surface. The above experimental results suggest that the PEC glucose sensor has been successfully fabricated step by step.

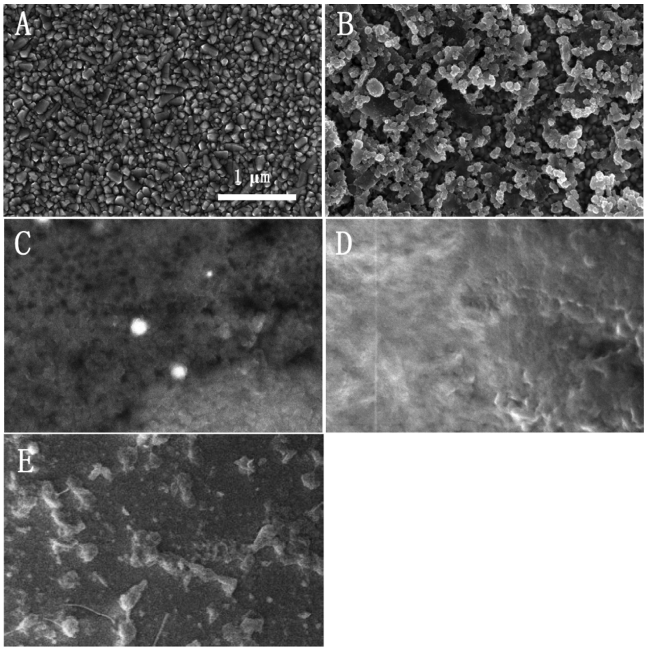

Figure 3. SEM images of (A) bare FTO, (B) calcined AuNR@TiO_2/FTO, (C) HRP−GOx−Au−PD/AuNR@TiO_2/FTO, and CS/HRP−GOx−Au−PD/AuNR@TiO_2/FTO electrodes (D) before and (E) after the BCP process with the same magnification.

Figure 4 shows the electrochemical and PEC characterizations of modified electrodes. Cyclic voltammetry (CV) and electrochemical impedance spectroscopy (EIS) responses of bare FTO, TiO_2/FTO, AuNR@TiO_2/FTO, HRP−GOx−Au−PD/AuNR@TiO_2/FTO, and CS/HRP−GOx−Au−PD/AuNR@TiO_2/FTO electrodes before and after the BCP process were obtained by using $K_4[Fe(CN)_6]$ as an electroactive probe (Figure 4A,B). EIS data are fitted to the Randles equivalent circuit (inset of Figure 4B). Compared with the redox peaks of bare FTO (0.263/0.124 V), the redox peaks on TiO_2/FTO shift to 0.285/0.096 V, which is consistent with the relatively poor electron transfer of the TiO_2 semiconductor and the findings of EIS. For AuNR@TiO_2/FTO, the current intensity is larger than that of bare FTO and TiO_2/FTO, accompanying with the decreases of peak-to-peak separation (ΔE_P) and the electron transfer resistance (R_{et}) obtained from EIS. These results indicate that the core−shell AuNR@TiO_2 possesses better electron-conductivity than TiO_2 because AuNR promotes the electron transfer process. Subsequently, HRP−GOx−Au−PD and then CS were introduced to the electrode surface, both leading to increased ΔE_P and R_{et} values (curves d and e) that imply the more difficult interfacial electron transfer. The current intensity was increased at HRP−GOx−Au−PD/AuNR@TiO_2/FTO, probably as a result of the good electron conductivity of Au nanoparticles in the HRP−GOx−Au−PD bionanocomposite. After the BCP process, ΔE_P and R_{et} values further increase, indicating the successful generation of electron-insulating precipitates on the electrode surface (curve f).

To investigate the detection feasibility of our proposed glucose enzymatic biosensor, PEC measurements were conducted in PBS containing 0.1 M AA as the electron donor, as shown in Figure 4C. After coating the HRP−GOx−Au−PD bionanocomposite on the AuNR@TiO_2/FTO electrode, the photocurrent density reaches to 162 μA cm^{-2} (curve a) because of the good light absorption of PD, Au nanoparticles, and HRP−GOx enzymes. Because of the poor electron conductivity of CS, the photocurrent density decreases to 143 μA cm^{-2} at the CS/HRP−GOx−Au−PD/AuNR@TiO_2/FTO electrode (curve b). After incubation with PBS containing 1 mM 4-chloro-1-naphthol and 0.1 mM glucose to complete the BCP process, a photocurrent density of 75.9 μA cm^{-2} (curve c) was obtained. Thus, the bienzyme-involved BCP strategy can realize the sensitive PEC detection of glucose. Figure S5 shows the good photostability of the CS/HRP−GOx−Au−PD/AuNR@TiO_2/FTO electrode by continuous ON/OFF light illumination. No apparent photocurrent changes were observed, suggesting the good stability of CS/HRP−GOx−Au−PD/AuNR@TiO_2/FTO.

To compare the performance of PD with PDA, a PDA-capsuled HRP−GOx−Au composite was prepared by the same procedures of HRP−GOx−Au−PD, except that 20 mM DA was used instead of 40 mM L-DOPA. The CS/HRP−GOx−

DOI: 10.1021/acsami.8b19284
ACS Appl. Mater. Interfaces 2019, 11, 9394−9404

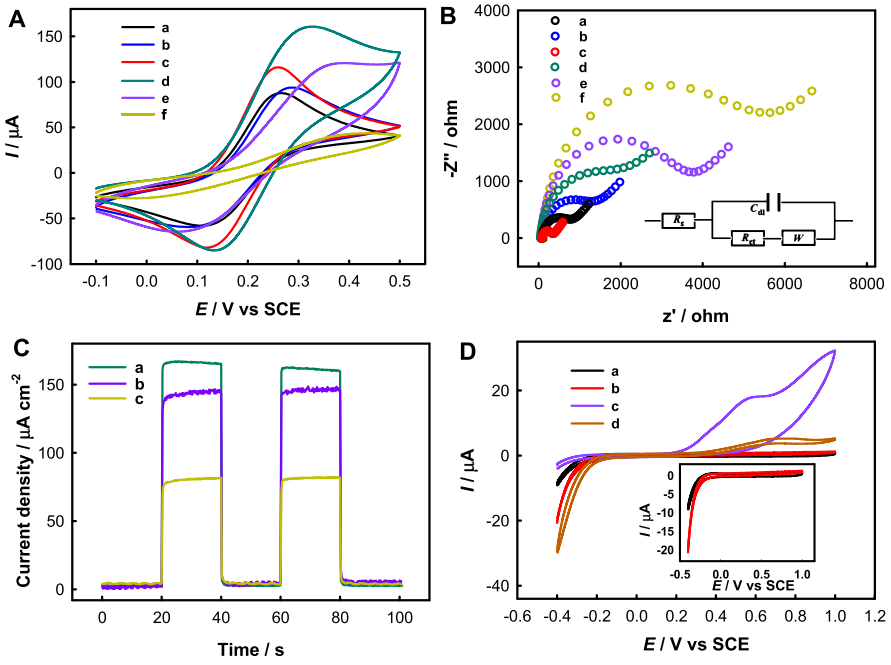

Figure 4. (A) CV and (B) EIS spectra of bare FTO (a), TiO_2/FTO (b), AuNR@TiO_2/FTO (c), HRP−GOx−Au−PD/AuNR@TiO_2/FTO (d), and CS/HRP−GOx−Au−PD/AuNR@TiO_2/FTO electrodes (e) before and (f) after the BCP process in PBS containing 2.0 mM $K_4Fe(CN)_6$ and 0.1 M Na_2SO_4. Scan rate: 50 mV s^{-1}. EIS experiments were conducted after biasing at 0.2 V for 200 s. (C) Photocurrent responses of (a) HRP−GOx−Au−PD/AuNR@TiO_2/FTO and CS/HRP−GOx−Au−PD/AuNR@TiO_2/FTO (b) before and (c) after the BCP process; the photoelectrodes were measured at a bias voltage of 0.1 V (vs SCE) in pH 7.0 PBS containing 0.1 M AA. (D) CV curves of bare FTO (a), AuNR@TiO_2/FTO (b), and CS/HRP−GOx−Au−PD/AuNR@TiO_2/FTO in the absence of glucose (c) and in the presence of 5.0 mM glucose (d) in 30.0 mM pH 7.0 PBS at a scan rate of 50 mV s^{-1}.

Au−PDA/AuNR@TiO_2/FTO electrode was used to detect 5 mM glucose by comparison, as shown in Figure S6. After BCP, the photocurrent density of the PDA-based electrode decreased by ca. 43.2%, while the PD-based electrode decreased by ca. 62.8%. The initial photocurrent intensity of the PD-based electrode is larger than that of the PDA-based electrode. It is reported that PD can be regarded as a special amino acid polymer (with an additional −COOH group vs DA), which possesses high biocompatibility and excellent adhesive ability for enzymes.[54] The oxidation polymerization of L-DOPA and DA is an indole-like polymerization mechanism. Because of the additional −COOH group on PD, the intermolecular cyclization process of PD and the cross-linking processes of the oxidized intermediates of PD can more easily occur than those of PDA, which can form big $\pi-\pi$ stacking that enhances the light absorption ability. Hence, PD can be regarded as a newly arising candidate instead of traditional DA-based polymers in the applications of photocatalysis and many PEC biosensors.

Figure 4D depicts the CV responses of bare FTO (curve a), AuNR@TiO_2/FTO (curve b), and CS/HRP−GOx−Au−PD/AuNR@TiO_2/FTO in the absence and the presence of 5 mM glucose (curves c and d) in pH 7.0 PBS. For bare FTO and AuNR@TiO_2/FTO, no peaks were observed because of the absence of redox species on the FTO surface. In contrast, CS/HRP−GOx−Au−PD/AuNR@TiO_2/FTO shows a single prominent oxidation peak around 0.56 V, which may correspond to the PD polymer in the HRP−GOx−Au−PD composite. In the presence of glucose, the characteristic peak of H_2O_2 at ca. 0.7 V was observed, indicating that GOx catalytic oxidation of glucose by O_2 produced H_2O_2.

The effects of (A) bias potential, (B) calcination time, and (C) the concentration of L-DOPA in the synthesis of HRP−GOx−Au−PD bionanocomposites were investigated to obtain the optimal performance of the glucose sensor, as shown in Figure S7. The bias potential is an important factor in correlation with photocurrent responses. Figure S7A depicts the photocurrent responses of CS/HRP−GOx−Au−PD/AuNR@TiO_2/FTO at different bias potentials. The maximum photocurrent was obtained at 0.1 V. Thus, the bias potential of 0.1 V was used in the subsequent experiments. The calcination time of AuNR@TiO_2/FTO was investigated in Figure S7B. The photocurrent increased with the increase of calcination time from 1 to 4 h and decreased at calcination for 5 h. Therefore, the optimal calcination time for AuNR@TiO_2/FTO is 4 h, which can turn the structure of amorphous TiO_2 into the anatase structure. Figure S7C shows the effect of L-DOPA concentration on the synthesis of the HRP−GOx−Au−PD bionanocomposite. The maximum photocurrent density of HRP−GOx−Au−PD/AuNR@TiO_2/FTO was obtained when the concentration of L-DOPA was 40 mM. Thus, 40 mM L-DOPA was chosen for the synthesis of HRP−GOx−Au−PD bionanocomposites.

Furthermore, we investigated the effects of the size of AuNR@TiO_2 core−shell nanorods on PEC and glucose-sensing performances, as shown in Figure S8. Figure S8A shows the UV−vis spectra of the prepared AuNRs with different longitudinal plasmon bands at (a) 648, (b) 707, (c) 745, (d) 843, and (e) 901 nm. To grow the longer AuNRs, we fixed the concentrations of gold ions and surfactants and changed the concentration of silver ions. It was reported that the length of the AuNRs increases with the increase of $AgNO_3$ concentration in the growth solution less than 0.12 mM.[66]

DOI: 10.1021/acsami.8b19284
ACS Appl. Mater. Interfaces 2019, 11, 9394−9404

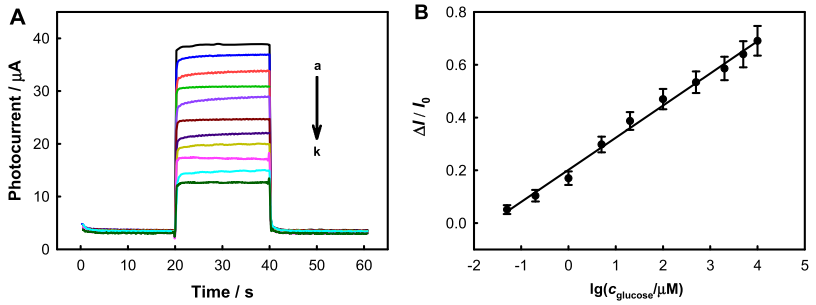

Figure 5. (A) Photocurrent responses for glucose at different concentrations [(a–k): blank, 0.05 μM, 0.2 μM, 1.0 μM, 5.0 μM, 20 μM, 100 μM, 500 μM, 2.0 mM, 5.0 mM, and 10.0 mM]. (B) Corresponding calibration curve. $\Delta I = I_0 - I$, where I_0 is the photocurrent of the modified electrode before BCP with glucose and I is the final photocurrent of the electrode after BCP. The photocurrent responses were measured in pH 7.0 PBS containing 0.1 M AA at 0.1 V.

Then, we prepared AuNR@TiO_2 core–shell nanorods of different sizes by using AuNRs of different longitudinal plasmon bands, varying from 648 to 901 nm (from a to e). As shown in Figure S8B, the optimal photocurrent density of AuNR@TiO_2 is obtained by using the AuNR of the longitudinal plasmon band at 843 nm (curve d). The longer AuNRs can incorporate the larger amount of Au in the TiO_2 shell, which can improve the charge separation and transfer of TiO_2. However, merely increasing the amount of AuNRs may passivate the light penetration and thus block the light available to the interfacial surface of TiO_2, resulting in the decrease of photocurrent.[38] It should be noted that the controlled synthesis of AuNR@TiO_2 can be realized by controlling the $NaHCO_3$ concentration and the pH value during the hydrolysis of $TiCl_3$.[66] Figure S8C shows the size effect of AuNR@TiO_2 nanorods on the glucose-sensing performance. As expected, we obtained better detection performance at a higher photovoltaic efficiency of the PEC photoelectrode. Thus, we chose the AuNR of the longitudinal plasmon band at 843 nm as the optimal size.

Under optimal conditions, glucose assay was carried out by time-dependent PEC photocurrent (i–t) measurements of CS/HRP–GOx–Au–PD/AuNR@TiO_2/FTO before and after BCP with glucose concentrations from 0.05 μM to 10.0 mM at 0.1 V in pH 7.0 PBS containing 0.1 M AA (Figure 5A). As the concentration of glucose increases, the photocurrent intensity decreases accordingly. The percentage of the photocurrent decrement is proportional to the common logarithm of glucose concentration in a linear range from 0.05 μM to 10.0 mM with a limit of detection of 0.01 μM (S/N = 3). The regression equation is $\Delta I/I_0 = 0.122 \lg c_{glucose}$ (μM) + 0.202 with a coefficient of 0.993 (Figure 5B). The possible mechanism for the PEC detection of glucose is as follows. With increasing glucose concentration, more H_2O_2 will be generated by GOx catalytic oxidation of glucose, which can catalyze the oxidation of more 4-chloro-1-naphthol in the presence of HRP to yield more precipitates on the transducer surface. Thus, the insulating precipitates reduced the photocurrent by obstructing the interfacial electron transfer of the electron donor (Scheme 1). Table S1 is the comparison of the present glucose detection method with some reported sensors, showing that the proposed CS/HRP–GOx–Au–PD/AuNR@TiO_2/FTO is a good platform for glucose detection.

The precision and reproducibility of the sensor were estimated by five parallel experiments to detect 0.1 mM glucose, the relative standard deviation is 4.1%, suggesting a satisfactory precision and reproducibility of this sensor to glucose detection. The chronic stability of this PEC enzymatic sensor was evaluated by storing CS/HRP–GOx–Au–PD/AuNR@TiO_2/FTO in a dark and humid environment at 4 °C for 25 days, and the photocurrent response was approximately 87.4% of its initial response, proving the good storage stability.

Furthermore, the specificity of the enzymatic sensor toward glucose was examined by mixing glucose with several possible interferents, including uric acid, acetaminophen, fructose, NaCl, and KCl. As shown in Figure S9, the detection signal in the presence of each of these substances and glucose only slightly changed in comparison with that of 0.1 mM glucose alone, indicating the good specificity of the sensor toward glucose detection.

To illustrate the potential applications of our sensor in practical analysis, CS/HRP–GOx–Au–PD/AuNR@TiO_2/FTO has been employed to analyze glucose in human blood serum samples. Before determination, the human blood serum samples were 50-fold diluted with pH 7.0 PBS to fit the wide linear detection range of the protocol. As listed in Table S2, the determined results of blood serum samples are in accordance with hospital results, and the recovery (between 97.4 and 107%) is acceptable, demonstrating the application potential of the proposed PEC enzymatic sensor for blood glucose assay.

4. CONCLUSIONS

A PD/AuNR@TiO_2 composite has been fabricated for the first time and characterized by TEM, UV, XRD, EDX, and IPCE. Owing to the good spectral properties of PD and AuNR, PD/AuNR@TiO_2 exhibits broadband light harvesting and high IPCE value than pristine TiO_2. The use of bioinspired PD as enzymes' coating film can simultaneously improve the PEC performance and biocompatibility of biosensing transducers. A novel PEC sensor for the sensitive detection of glucose on the CS/HRP–GOx–Au–PD/AuNR@TiO_2/FTO electrode has been fabricated, which shows a low LOD (0.01 μM) and a wide linear range (0.05 μM to 10.0 mM) to detect glucose. The developed high-performance photocatalyst and biosensing platform may be of some general value for designing other biosensing platforms and exploiting other PEC applications.

■ ASSOCIATED CONTENT

Supporting Information

The Supporting Information is available free of charge on the ACS Publications website at DOI: 10.1021/acsami.8b19284.

XRD patterns; electron transfer mechanism of the PEC transducer; UV–vis spectra of PD/FTO, AuNR@TiO_2/

DOI: 10.1021/acsami.8b19284
ACS Appl. Mater. Interfaces 2019, 11, 9394–9404

FTO, and PD/AuNR@TiO_2/FTO; TEM image of the HRP-GOx-Au-PD bionanocomposite; UV−vis spectra of aqueous solutions/dispersion; photostability of CS/HRP-GOx-Au-PD/AuNR@TiO_2/FTO; photocurrent responses; effects of bias potential, calcination time, and concentration of L-DOPA; UV−vis spectra of AuNRs; photocurrent responses for AuNR@TiO_2 core-shell nanorods of different sizes; photocurrent responses on CS/HRP-GOx-Au-PD/AuNR@TiO_2/FTO before (solid lines) and after (dotted black lines) the BCP process; detection signal of 0.1 mM uric acid acetaminophen, fructose, NaCl, or KCl; comparison of analytical performances between the proposed sensor and other sensors; and determination of glucose concentration (PDF)

AUTHOR INFORMATION

Corresponding Authors

*E-mail: xieqj@hunnu.edu.cn. Phone: +86-731-88865515 (Q.X.).

*E-mail: lyl56@126.com (Y.L.).

ORCID

Yueming Tan: 0000-0003-3356-9079

Qingji Xie: 0000-0001-7860-446X

Notes

The authors declare no competing financial interest.

ACKNOWLEDGMENTS

This work was supported by the National Natural Science Foundation of China (21675050, 21475041), Hunan Lotus Scholars Program (2011), and Foundations of the Education Department and the Science & Technology Department of Hunan Province (14C0712, 2016SK2020).

REFERENCES

(1) Chen, C.; Xie, Q.; Yang, D.; Xiao, H.; Fu, Y.; Tan, Y.; Yao, S. Recent Advances in Electrochemical Glucose Biosensors: A Review. *RSC Adv.* **2013**, *3*, 4473−4491.

(2) Wang, J. Electrochemical Glucose Biosensors. *Chem. Rev.* **2008**, *108*, 814−825.

(3) Sulak, M. T.; Gökdoğan, Ö.; Gülce, A.; Gülce, H. Amperometric Glucose Biosensor Based on Gold-Deposited Polyvinylferrocene Film on Pt Electrode. *Biosens. Bioelectron.* **2006**, *21*, 1719−1726.

(4) Zhao, W.-W.; Xu, J.-J.; Chen, H.-Y. Photoelectrochemical Bioanalysis: The State of the Art. *Chem. Soc. Rev.* **2015**, *44*, 729−741.

(5) Fan, G.-C.; Han, L.; Zhu, H.; Zhang, J.-R.; Zhu, J.-J. Ultrasensitive Photoelectrochemical Immunoassay for Matrix Metalloproteinase-2 Detection Based on CdS:Mn/CdTe Cosensitized TiO_2 Nanotubes and Signal Amplification of SiO_2@Ab_2 Conjugates. *Anal. Chem.* **2014**, *86*, 12398−12405.

(6) Wang, L.; Ma, W.; Gan, S.; Han, D.; Zhang, Q.; Niu, L. Engineered Photoelectrochemical Platform for Rational Global Antioxidant Capacity Evaluation Based on Ultrasensitive Sulfonated Graphene−TiO_2 Nanohybrid. *Anal. Chem.* **2014**, *86*, 10171−10178.

(7) Devadoss, A.; Sudhagar, P.; Terashima, C.; Nakata, K.; Fujishima, A. Photoelectrochemical Biosensors: New Insights into Promising Photoelectrodes and Signal Amplification Strategies. *J. Photochem. Photobiol., C* **2015**, *24*, 43−63.

(8) Wang, L.; Zhu, W.; Lu, W.; Qin, X.; Xu, X. Surface Plasmon Aided High Sensitive Non-Enzymatic Glucose Sensor Using Au/NiAu Multilayered Nanowire Arrays. *Biosens. Bioelectron.* **2018**, *111*, 41−46.

(9) Yang, Y.; Yan, K.; Zhang, J. Dual Non-Enzymatic Glucose Sensing on $Ni(OH)_2$/TiO_2 Photoanode under Visible Light Illumination. *Electrochim. Acta* **2017**, *228*, 28−35.

(10) Gopalan, A.; Muthuchamy, N.; Lee, K. A Novel Bismuth Oxychloride-Graphene Hybrid Nanosheets Based Non-Enzymatic Photoelectrochemical Glucose Sensing Platform for High Performances. *Biosens. Bioelectron.* **2017**, *89*, 352−360.

(11) Devadoss, A.; Sudhagar, P.; Ravidhas, C.; Hishinuma, R.; Terashima, C.; Nakata, K.; Kondo, T.; Shitanda, I.; Yuasa, M.; Fujishima, A. Simultaneous Glucose Sensing and Biohydrogen Evolution from Direct Photoelectrocatalytic Glucose Oxidation on Robust Cu_2O−TiO_2 Electrodes. *Phys. Chem. Chem. Phys.* **2014**, *16*, 21237−21242.

(12) Zhang, X.; Huo, K.; Peng, X.; Xu, R.; Li, P.; Chen, R.; Zheng, G.; Wu, Z.; Chu, P. K. WO_3 Nanoparticles Decorated Core−Shell TiC−C Nanofiber Arrays for High Sensitive and Non-Enzymatic Photoelectrochemical Biosensing. *Chem. Commun.* **2013**, *49*, 7091−7093.

(13) Chen, D.; Jiang, D.; Du, X.; Zhou, L.; Huang, L.; Qian, J.; Liu, Q.; Hao, N.; Li, Y.; Wang, K. Engineering Efficient Charge Transfer Based on Ultrathin Graphite-Like Carbon Nitride/WO_3 Semiconductor Nanoheterostructures for Fabrication of High-Performances Non-Enzymatic Photoelectrochemical Glucose Sensor. *Electrochim. Acta* **2016**, *215*, 305−312.

(14) Huo, H.; Xu, Z.; Zhang, T.; Xu, C. Ni/CdS/TiO_2 Nanotube Array Heterostructures for High Performance Photoelectrochemical Biosensing. *J. Mater. Chem. A* **2015**, *3*, 5882−5888.

(15) Shang, M.; Qi, H.; Du, C.; Huang, H.; Wu, S.; Zhang, J.; Song, W. One-Step Electrodeposition of High-Quality Amorphous Molybdenum Sulfide/RGO Photoanode for Visible-Light Sensitive Photoelectrochemical Biosensing. *Sens. Actuators, B* **2018**, *266*, 71−79.

(16) Zhao, W.-W.; Xu, J.-J.; Chen, H.-Y. Photoelectrochemical Enzymatic Biosensors. *Biosens. Bioelectron.* **2017**, *92*, 294−304.

(17) Hou, T.; Zhang, L.; Sun, X.; Li, F. Biphasic Photoelectrochemical Sensing Strategy Based on in Situ Formation of Cds Quantum Dots for Highly Sensitive Detection of Acetylcholinesterase Activity and Inhibition. *Biosens. Bioelectron.* **2016**, *75*, 359−364.

(18) Yan, Z.; Wang, Z.; Miao, Z.; Liu, Y. Dye-Sensitized and Localized Surface Plasmon Resonance Enhanced Visible-Light Photoelectrochemical Biosensors for Highly Sensitive Analysis of Protein Kinase Activity. *Anal. Chem.* **2016**, *88*, 922−929.

(19) Du, J.; Yu, X.; Wu, Y.; Di, J. ZnS Nanoparticles Electrodeposited onto ITO Electrode as a Platform for Fabrication of Enzyme-Based Biosensors of Glucose. *Mater. Sci. Eng., C* **2013**, *33*, 2031−2036.

(20) Zhang, X.; Liu, M.; Liu, H.; Zhang, S. Low-Toxic Ag_2S Quantum Dots for Photoelectrochemical Detection Glucose and Cancer Cells. *Biosens. Bioelectron.* **2014**, *56*, 307−312.

(21) Ertek, B.; Akgül, C.; Dilgin, Y. Photoelectrochemical Glucose Biosensor Based on a Dehydrogenase Enzyme and NAD^+/NADH Redox Couple Using a Quantum Dot Modified Pencil Graphite Electrode. *RSC Adv.* **2016**, *6*, 20058−20066.

(22) Song, Z.; Fan, G.-C.; Li, Z.; Gao, F.; Luo, X. Universal Design of Selectivity-Enhanced Photoelectrochemical Enzyme Sensor: Integrating Photoanode with Biocathode. *Anal. Chem.* **2018**, *90*, 10681−10687.

(23) Zhao, Y.; Gong, J.; Zhang, X.; Kong, R.; Qu, F. Enhanced Biosensing Platform Constructed Using Urchin-Like ZnO-Au@CdS Microspheres Based on the Combination of Photoelectrochemical and Bioetching Strategies. *Sens. Actuators, B* **2018**, *255*, 1753−1761.

(24) Liu, X.; Huo, X.; Liu, P.; Tang, Y.; Xu, J.; Liu, X.; Zhou, Y. Assembly of MoS_2 Nanosheet-TiO_2 Nanorod Heterostructure as Sensor Scaffold for Photoelectrochemical Biosensing. *Electrochim. Acta* **2017**, *242*, 327−336.

(25) Fujishima, A.; Honda, K. Electrochemical Photolysis of Water at a Semiconductor Electrode. *Nature* **1972**, *238*, 37−38.

(26) Hashimoto, K.; Irie, H.; Fujishima, A. TiO_2 Photocatalysis: A Historical Overview and Future Prospects. *Jpn. J. Appl. Phys.* **2005**, *44*, 8269−8285.

DOI: 10.1021/acsami.8b19284
ACS Appl. Mater. Interfaces 2019, 11, 9394−9404

(27) Tang, J.; Wang, Y.; Li, J.; Da, P.; Geng, J.; Zheng, G. Sensitive Enzymatic Glucose Detection by TiO_2 Nanowire Photoelectrochemical Biosensors. *J. Mater. Chem. A* **2014**, *2*, 6153−6157.
(28) Li, X.; Yao, J.; Liu, F.; He, H.; Zhou, M.; Mao, N.; Xiao, P.; Zhang, Y. Nickel/Copper Nanoparticles Modified TiO_2 Nanotubes for Non-Enzymatic Glucose Biosensors. *Sens. Actuators, B* **2013**, *181*, 501−508.
(29) Çakıroğlu, B.; Özacar, M. A Self-Powered Photoelectrochemical Glucose Biosensor Based on Supercapacitor Co_3O_4-CNT Hybrid on TiO_2. *Biosens. Bioelectron.* **2018**, *119*, 34−41.
(30) Shaban, M.; Ashraf, A. M.; Abukhadra, M. R. TiO_2 Nanoribbons/Carbon Nanotubes Composite with Enhanced Photocatalytic Activity; Fabrication, Characterization, and Application. *Sci. Rep.* **2018**, *8*, 781.
(31) Ma, X.; Wu, Y.; Lu, Y.; Xu, J.; Wang, Y.; Zhu, Y. Effect of Compensated Codoping on the Photoelectrochemical Properties of Anatase TiO_2 Photocatalyst. *J. Phys. Chem. C* **2011**, *115*, 16963−16969.
(32) Sousa-Castillo, A.; Comesaña-Hermo, M.; Rodríguez-González, B.; Pérez-Lorenzo, M.; Wang, Z.; Kong, X.-T.; Govorov, A. O.; Correa-Duarte, M. A. Boosting Hot Electron-Driven Photocatalysis through Anisotropic Plasmonic Nanoparticles with Hot Spots in Au−TiO_2 Nanoarchitectures. *J. Phys. Chem. C* **2016**, *120*, 11690−11699.
(33) Chandrasekharan, N.; Kamat, P. V. Improving the Photoelectrochemical Performance of Nanostructured TiO_2 Films by Adsorption of Gold Nanoparticles. *J. Phys. Chem. B* **2000**, *104*, 10851−10857.
(34) Ma, L.; Chen, K.; Nan, F.; Wang, J.-H.; Yang, D.-J.; Zhou, L.; Wang, Q.-Q. Improved Hydrogen Production of Au-Pt-CdS Heterostructures by Efficient Plasmon-Induced Multipathway Electron Transfer. *Adv. Funct. Mater.* **2016**, *26*, 6076−6083.
(35) Guo, L.; Li, Z.; Marcus, K.; Navarro, S.; Liang, K.; Zhou, L.; Mani, P. D.; Florczyk, S. J.; Coffey, K. R.; Orlovskaya, N.; Sohn, Y.-H.; Yang, Y. Periodically Patterned Au-TiO_2 Heterostructures for Photoelectrochemical Sensor. *ACS Sens.* **2017**, *2*, 621−625.
(36) Wang, X.; Xia, X.; Zhang, X.; Meng, W.; Yuan, C.; Guo, M. Nonenzymatic Glucose Sensor Based on Ag&Pt Hollow Nanoparticles Supported on TiO_2 Nanotubes. *Mater. Sci. Eng., C* **2017**, *80*, 174−179.
(37) Wang, Y.; Chen, J.; Zhou, C.; Zhou, L.; Kong, Y.; Long, H.; Zhong, S. A Novel Self-Cleaning, Non-Enzymatic Glucose Sensor Working under a Very Low Applied Potential Based on a Pt Nanoparticle-Decorated TiO_2 Nanotube Array Electrode. *Electrochim. Acta* **2014**, *115*, 269−276.
(38) Devadoss, A.; Sudhagar, P.; Das, S.; Lee, S. Y.; Terashima, C.; Nakata, K.; Fujishima, A.; Choi, W.; Kang, Y. S.; Paik, U. Synergistic Metal-Metal Oxide Nanoparticles Supported Electrocatalytic Graphene for Improved Photoelectrochemical Glucose Oxidation. *ACS Appl. Mater. Interfaces* **2014**, *6*, 4864−4871.
(39) Wang, Y.; Bai, L.; Wang, Y.; Qin, D.; Shan, D.; Lu, X. Ternary Nanocomposites of Au/CuS/TiO_2 for an Ultrasensitive Photoelectrochemical Non-Enzymatic Glucose Sensor. *Analyst* **2018**, *143*, 1699−1704.
(40) Li, J.-F.; Zhang, Y.-J.; Ding, S.-Y.; Panneerselvam, R.; Tian, Z.-Q. Core-Shell Nanoparticle-Enhanced Raman Spectroscopy. *Chem. Rev.* **2017**, *117*, 5002−5069.
(41) Chen, H.; Shao, L.; Li, Q.; Wang, J. Gold Nanorods and Their Plasmonic Properties. *Chem. Soc. Rev.* **2013**, *42*, 2679−2724.
(42) Zheng, Z.; Tachikawa, T.; Majima, T. Single-Particle Study of Pt-Modified Au Nanorods for Plasmon-Enhanced Hydrogen Generation in Visible to near-Infrared Region. *J. Am. Chem. Soc.* **2014**, *136*, 6870−6873.
(43) Pu, Y.-C.; Wang, G.; Chang, K.-D.; Ling, Y.; Lin, Y.-K.; Fitzmorris, B. C.; Liu, C.-M.; Lu, X.; Tong, Y.; Zhang, J. Z.; Hsu, Y.-J.; Li, Y. Au Nanostructure-Decorated TiO_2 Nanowires Exhibiting Photoactivity across Entire UV-Visible Region for Photoelectrochemical Water Splitting. *Nano Lett.* **2013**, *13*, 3817−3823.
(44) Lee, B. P.; Messersmith, P. B.; Israelachvili, J. N.; Waite, J. H. Mussel-Inspired Adhesives and Coatings. *Annu. Rev. Mater. Res.* **2011**, *41*, 99−132.
(45) Lee, H.; Dellatore, S. M.; Miller, W. M.; Messersmith, P. B. Mussel-Inspired Surface Chemistry for Multifunctional Coatings. *Science* **2007**, *318*, 426−430.
(46) Meredith, P.; Sarna, T. The Physical and Chemical Properties of Eumelanin. *Pigm. Cell Res.* **2006**, *19*, 572−594.
(47) Nam, H. J.; Kim, B.; Ko, M. J.; Jin, M.; Kim, J. M.; Jung, D.-Y. A New Mussel-Inspired Polydopamine Sensitizer for Dye-Sensitized Solar Cells: Controlled Synthesis and Charge Transfer. *Chem.—Eur. J.* **2012**, *18*, 14000−14007.
(48) Zhang, X.; Wang, S.; Xu, L.; Feng, L.; Ji, Y.; Tao, L.; Li, S.; Wei, Y. Biocompatible Polydopamine Fluorescent Organic Nanoparticles: Facile Preparation and Cell Imaging. *Nanoscale* **2012**, *4*, 5581−5584.
(49) Wang, Z.; Li, J.; Tang, F.; Lin, J.; Jin, Z. Polydopamine Nanotubes-Templated Synthesis of TiO_2 and Its Photocatalytic Performance under Visible Light. *RSC Adv.* **2017**, *7*, 23535−23542.
(50) Li, W.; Zhang, G.; Sheng, W.; Dong, C.; Dai, Y.; Li, C.; Wang, R.; Shi, Y.; Guo, X.; Jia, X. Engineering Plasmonic Ag/AgCl-Polydopamine-Carbon Nitride Composites for Enhanced Photocatalytic Activity Based on Mussel Chemistry. *RSC Adv.* **2016**, *6*, 106697−106704.
(51) Ryu, G. M.; Lee, M.; Choi, D. S.; Park, C. B. A Hematite-Based Photoelectrochemical Platform for Visible Light-Induced Biosensing. *J. Mater. Chem. B* **2015**, *3*, 4483−4486.
(52) Nam, H. J.; Kim, B.; Ko, M. J.; Jin, M.; Kim, J. M.; Jung, D.-Y. A New Mussel-Inspired Polydopamine Sensitizer for Dye-Sensitized Solar Cells: Controlled Synthesis and Charge Transfer. *Chem.—Eur. J.* **2012**, *18*, 14000−14007.
(53) Mason, H. S. The Chemistry of Melanin: Iii. Mechanism of the Oxidation of Dihydroxyphenylalanine by Tyrosinase. *J. Biol. Chem.* **1948**, *172*, 83−99.
(54) Dai, M.; Sun, L.; Chao, L.; Tan, Y.; Fu, Y.; Chen, C.; Xie, Q. Immobilization of Enzymes by Electrochemical and Chemical Oxidative Polymerization of L-DOPA to Fabricate Amperometric Biosensors and Biofuel Cells. *ACS Appl. Mater. Interfaces* **2015**, *7*, 10843−10852.
(55) Shi, Y.; Liu, M.; Deng, F.; Zeng, G.; Wan, Q.; Zhang, X.; Wei, Y. Recent Progress and Development on Polymeric Nanomaterials for Photothermal Therapy: A Brief Overview. *J. Mater. Chem. B* **2017**, *5*, 194−206.
(56) Zadlo, A.; Burke, J. M.; Sarna, T. Effect of Untreated and Photobleached Bovine Rpe Melanosomes on the Photoinduced Peroxidation of Lipids. *Photochem. Photobiol. Sci.* **2009**, *8*, 830−837.
(57) Kollias, N.; Sayre, R. M.; Zeise, L.; Chedekel, M. R. New Trends in Photobiology. *J. Photochem. Photobiol., B* **1991**, *9*, 135−160.
(58) Dai, M.; Huang, T.; Chao, L.; Tan, Y.; Chen, C.; Meng, W.; Xie, Q. Tyrosinase-catalyzed polymerization of l-DOPA (versusl-tyrosine and dopamine) to generate melanin-like biomaterials for immobilization of enzymes and amperometric biosensing. *RSC Adv.* **2016**, *6*, 17016−17022.
(59) Kobayashi, S.; Makino, A. Enzymatic Polymer Synthesis: An Opportunity for Green Polymer Chemistry. *Chem. Rev.* **2009**, *109*, 5288−5353.
(60) Tanne, J.; Schäfer, D.; Khalid, W.; Parak, W. J.; Lisdat, F. Light-Controlled Bioelectrochemical Sensor Based on CdSe/ZnS Quantum Dots. *Anal. Chem.* **2011**, *83*, 7778−7785.
(61) Sun, J.; Zhu, Y.; Yang, X.; Li, C. Photoelectrochemical Glucose Biosensor Incorporating CdS Nanoparticles. *Particuology* **2009**, *7*, 347−352.
(62) Zhao, C.; Zhang, Z.; Zhao, Y.; Yu, J. Photoelectrochemical Detection of Glucose by Using an Enzyme-Modified Photoelectrode. *Chin. J. Chem.* **2012**, *30*, 1851−1856.
(63) Sheng, Q.; Zheng, J. Bienzyme System for the Biocatalyzed Deposition of Polyaniline Templated by Multiwalled Carbon Nanotubes: A Biosensor Design. *Biosens. Bioelectron.* **2009**, *24*, 1621−1628.

DOI: 10.1021/acsami.8b19284
ACS Appl. Mater. Interfaces 2019, 11, 9394−9404

(64) Patolsky, F.; Zayats, M.; Katz, E.; Willner, I. Precipitation of an Insoluble Product on Enzyme Monolayer Electrodes for Biosensor Applications: Characterization by Faradaic Impedance Spectroscopy, Cyclic Voltammetry, and Microgravimetric Quartz Crystal Microbalance Analyses. *Anal. Chem.* **1999**, *71*, 3171−3180.
(65) Ong, W.-J.; Tan, L.-L.; Ng, Y. H.; Yong, S.-T.; Chai, S.-P. Graphitic Carbon Nitride ($g\text{-}C_3N_4$)-Based Photocatalysts for Artificial Photosynthesis and Environmental Remediation: Are We a Step Closer to Achieving Sustainability? *Chem. Rev.* **2016**, *116*, 7159−7329.
(66) Nikoobakht, B.; El-Sayed, M. A. Preparation and Growth Mechanism of Gold Nanorods (NRS) Using Seed-Mediated Growth Method. *Chem. Mater.* **2003**, *15*, 1957−1962.
(67) Liu, J.; Hu, X.; Hou, S.; Wen, T.; Liu, W.; Zhu, X.; Yin, J.-J.; Wu, X. Au@Pt Core/Shell Nanorods with Peroxidase- and Ascorbate Oxidase-Like Activities for Improved Detection of Glucose. *Sens. Actuators, B* **2012**, *166−167*, 708−714.
(68) Fang, C.; Jia, H.; Chang, S.; Ruan, Q.; Wang, P.; Chen, T.; Wang, J. (Gold Core)/(Titania Shell) Nanostructures for Plasmon-Enhanced Photon Harvesting and Generation of Reactive Oxygen Species. *Energy Environ. Sci.* **2014**, *7*, 3431−3438.
(69) Bisquert, J.; Zaban, A.; Greenshtein, M.; Mora-Seró, I. Determination of Rate Constants for Charge Transfer and the Distribution of Semiconductor and Electrolyte Electronic Energy Levels in Dye-Sensitized Solar Cells by Open-Circuit Photovoltage Decay Method. *J. Am. Chem. Soc.* **2004**, *126*, 13550−13559.

DOI: 10.1021/acsami.8b19284
ACS Appl. Mater. Interfaces 2019, 11, 9394−9404